Chandra Calibration Memo - July 20, 2008

Cross-Calibration of Cluster Temperatures between Chandra and XMM-Newton

1. Initial Results

As part of a on-going project with the Astronomical International Council for High Energy Calibration (IACHEC), we compiled a sample of 7 clusters of galaxies (see Table 1) to compare gas temperatures derived from ACIS, MOS and PN data. All of the selected clusters are relaxed systems and most have cool cores. In general, cool core clusters have a positive temperature gradient at small radii, attain a peak temperature between 50 and 200 kpc, and have a declining temperature at larger radii. For our study, we extracted spectra in annular regions near the peak of the temperature profile. Since the imaging properties of XMM-Newton and Chandra are very different, care must be taken to ensure that the XMM-Newton results are not affected by the scattering of emission from the cool cores into the outer annular regions used for cross-calibration. We therefore extracted ACIS surface brightness profiles for each cluster. Combining these surface brightness profiles with analytic expressions for the XMM PSF, we were able to estimate the effects of scattering in our spectral analysis of the XMM-Newton data.

When this project began, revisions to the low energy response of the two MOS detectors (to improve cross-calibration with RGS1) were imminent, so we restricted our comparison to the 2.0-7.0 keV band pass. Since that time, all of the XMM-Newton data have been reprocessed with SASS 7.1. The resulting comparison between ACIS, MOS and PN derived temperatures in 2.0-7.0 keV energy band are shown in Figs. 1-3 using CIAO 4.0.2 and CALDB 3.4.5 for the Chandra data analysis and SASS 7.1 for the XMM-Newton data analysis. A comparison of ACIS, MOS and PN derived temperatures in an energy band more commonly used by observers (0.5-7.0 keV) is shown in Fig. 4. The temperatures are obtained by fitting the spectra with a single absorbed thermal model (mekal) with the absorption fixed at the galactic value (see Table 1).

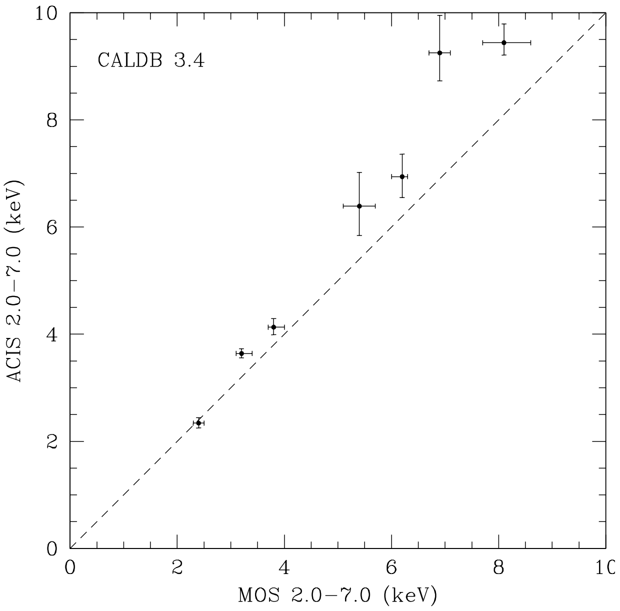

Fig. 1. A comparison between ACIS and MOS derived cluster temperatures in the 2.0-7.0 keV band. Error bars are shown at the 1σ confidence level.

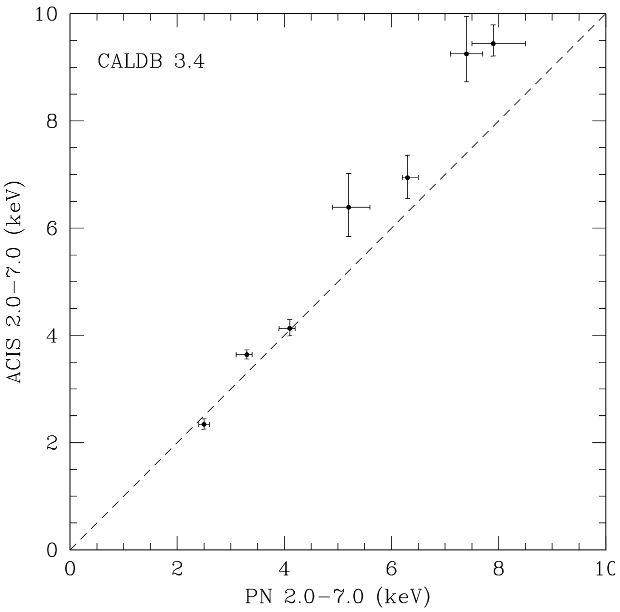

Fig. 2. A comparison between ACIS and PN derived cluster temperatures in the 2.0-7.0 keV band. Error bars are shown at the 1σ confidence level.

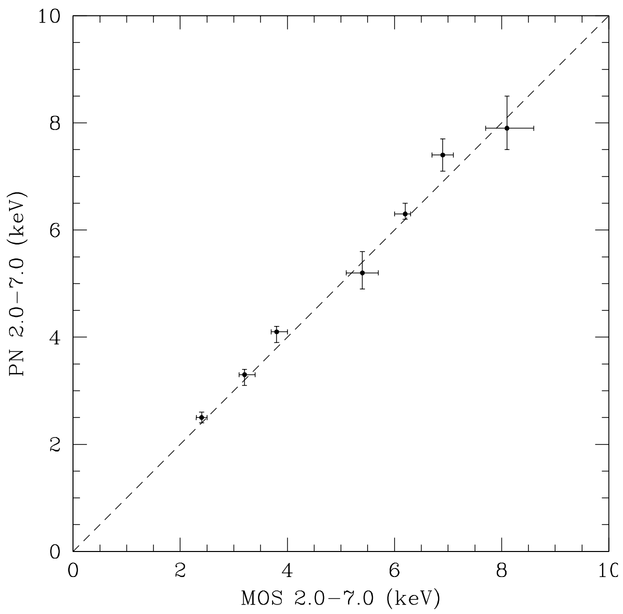

Fig 3. A comparison between PN and MOS derived cluster temperatures in the 2.0-7.0 keV band. Error bars are shown at the 1σ confidence level.

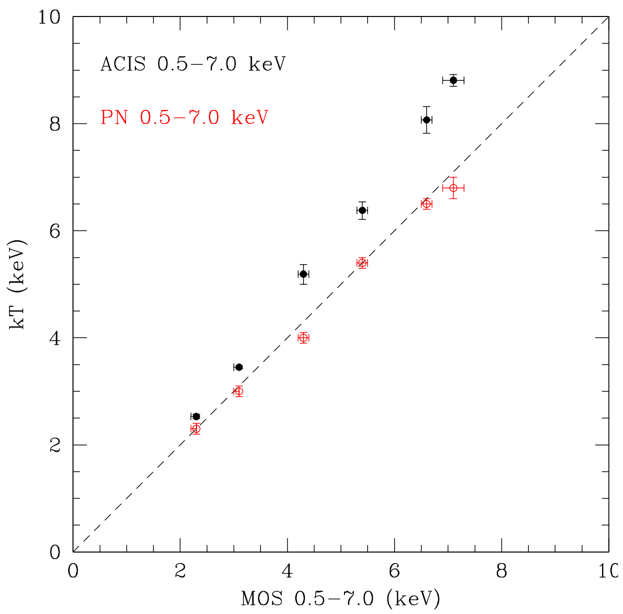

Fig 4. A comparison between ACIS, MOS and PN derived cluster temperatures in the 0.5-7.0 keV band. The ACIS temperatures are shown as filled circles and the PN temperatures are shown as open circles. Error bars are shown at the 1σ confidence level.

Figs. 1-4 show that the gas temperatures derived from MOS and PN are in agreement over the full range of cluster temperatures. Below 4 keV, ACIS temperatures are also in agreement with PN and MOS cluster temperature. However, above 4 keV, ACIS temperatures are 10-20% greater than PN and MOS derived temperatures.

Since it is impossible to determine from such a comparison which temperature is closest to the true temperature, we decided to check the internal consistency of the HRMA/ACIS calibration by comparing temperatures obtained from fitting different energy bands. Fig. 5 shows the temperatures derived from fitting a broad energy band (0.5-7.0 keV) and a hard energy band (2.0-7.0 keV). This figure shows that the temperatures obtained by fitting the hard energy band are greater than the temperatures obtained by fitting the broad energy band for clusters hotter than about 4 keV. Of course, since we are fitting the projected emission through a cluster atmosphere which has a non-isothermal temperature profile, this result alone does not indicate a problem with the Chandra calibration. To determine if the projected spectrum in an annulus near the peak temperature in a cluster should be well represented by a single thermal plasma model, we simulated a projected 6-temperature spectrum of the annular region fitted in Abell 2029 based on the density and temperature profiles in Vikhlinin et al. (2006). We then fitted the simulated 6-temperature spectrum to a single thermal plasma model and obtained consistent temperatures in the broad and hard energy bands.

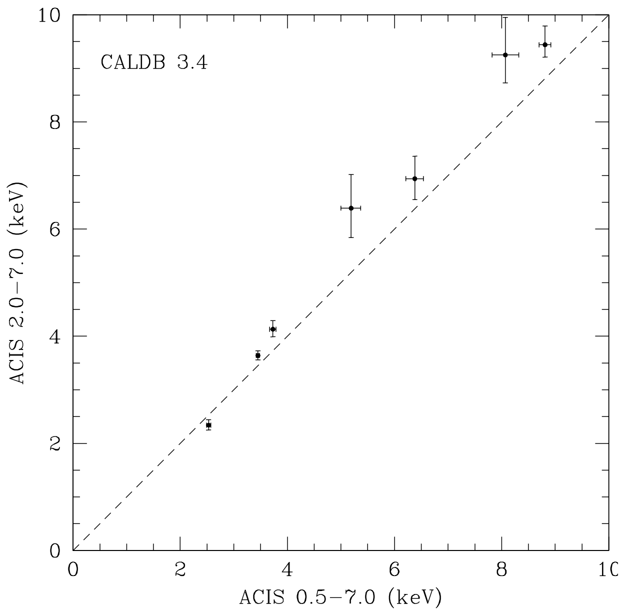

Fig. 5. A comparison between ACIS derived cluster temperatures in the 2.0-7.0 keV energy band and 0.5-7.0 keV energy band. Error bars are shown at the 1σ confidence level.

To further check the internal consistency of the HRMA/ACIS calibration, we compared the temperature derived in the 2.0-6.0 keV energy band (which is mostly continuum emission for the hotter clusters) with the temperature derived from the the H-like to He-like Fe-kα line ratio (see Fig. 6). The temperature derived from the Fe line ratio is fairly insensitive to calibration uncertainties (i.e., a systematic uncertainty in the slope of the effective area will not affect the line strength ratio of two lines at nearly the same energy).

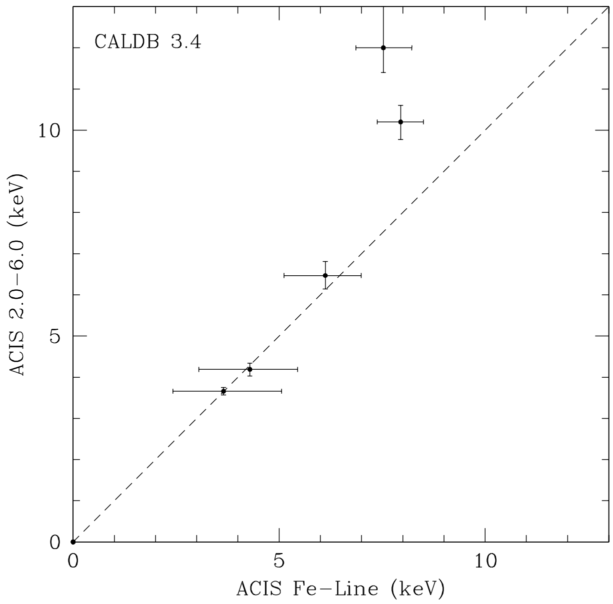

Fig. 6. A comparison between ACIS derived cluster temperatures in the 2.0-6.0 keV energy band and the temperature derived from the H-like to He-like Fe-Kα line ratio.

This figure shows that the temperatures derived from the the 2.0-6.0 keV continuum are greater than the temperatures determined from the Fe line ratio in clusters hotter than about 5 keV.

2. HRMA Effective Area Calibration

Since the discrepancies in the temperatures derived from fitting different energy bands are consistent between ACIS-I3 and ACIS-S3 data, we re-examined the calibration of the High Resolution Mirror Assembly (HRMA) on-board Chandra. There have been two major adjustments to the effective area of the HRMA. The first was an empirical correction based on the results of extensive ground-based tests at the X-Ray Calibration Facility (XRCF) at the Marshall Space Flight Center (MSFC).

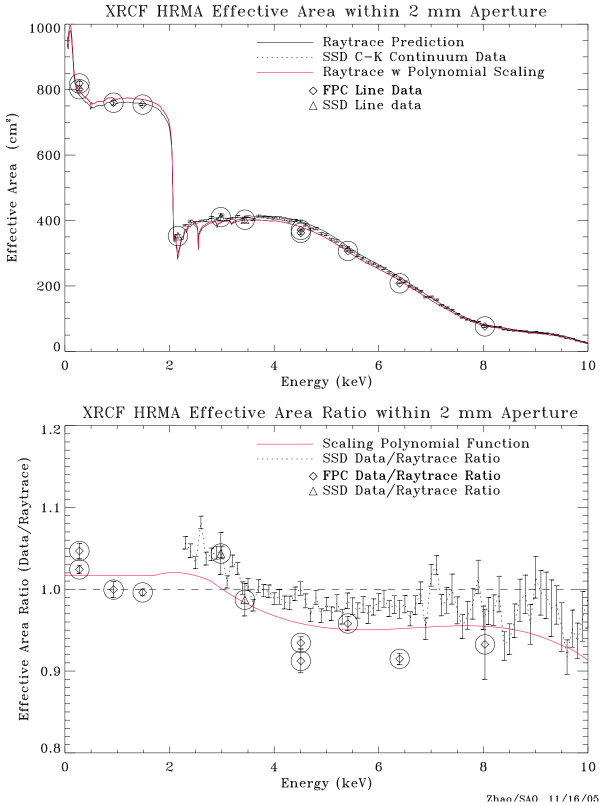

Fig. 7. SAOSAC raytrace code predictions for the HRMA effective area at XRCF along with ground-based measurements.

The top panel of Fig. 7 shows the predictions for the HRMA effective area based on the SAOSAC ray trace code (solid line) along with emission-line measurements using a flow proportional counter (FPC) and a solid-state detector (SSD) at the aim-point. The nearly continuous set of data points above 2 keV shows the effective area as measured with a continuum source and the SSD. The bottom panel of Fig. 8 shows the difference between the ray trace predictions for the HRMA effective area (normalized to unity at all energies) and the XRCF measurements. The red curve is a fourth order polynomial fit to the XRCF measurements. This fourth order polynomial fit was applied to the predictions of the ray trace code to generate a HRMA effective area file for in-flight data. This corresponds to version N0006 in the CALDB and was the default version prior to CALDB 3.2.1 released on Dec. 15, 2005.

After launch, analysis of gratings data showed that there were residuals in the spectra of blazars near the Ir-M edge of the mirrors. A grid of HRMA effective area models were then generated with a hydrocarbon overlayer on the mirrors and a range of depths. Fig. 8 shows that the residuals in the gratings spectra near the Ir-M edge are essentially removed if the mirrors have a hydrocarbon overlayer with a thickness of approximately 22 Å. This result lead to the release of version N0007 of the HRMA effective area file in CALDB 3.2.1 and has been the default version since that time.

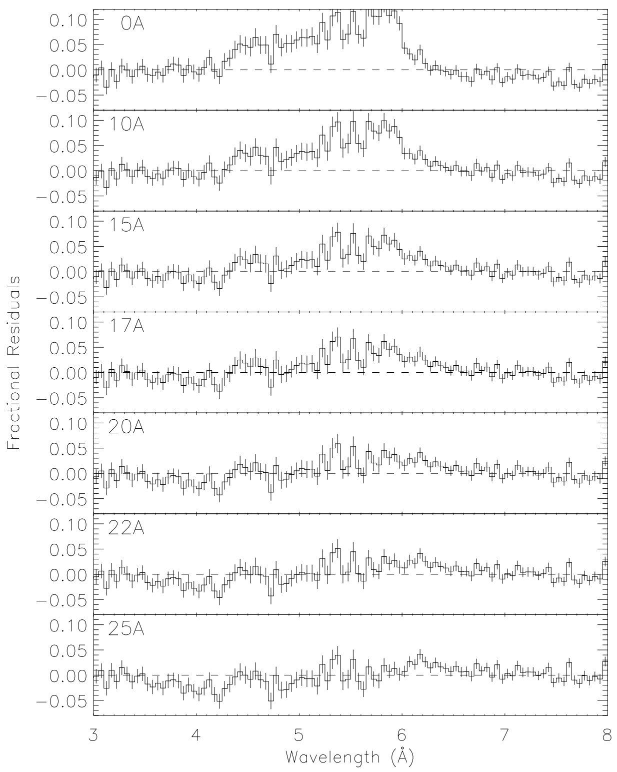

Fig. 8. HETG/ACIS-S gratings data of the combined emission from 13 blazars fitted to HRMA effective area models with a range of depths for a hydrocarbon overlayer.

The effects of a hydrocarbon overlayer on the HRMA effective area are shown in Fig. 9. Notice that the increase in effective area is the greatest at, and slightly above, the Ir-M edge. A comparison of Figs. 7 and 9 shows that the shape of the SSD continuum measurement at the XRCF and the effects of an overlayer on the mirrors are very similar above 2 keV, suggesting that the overlayer was already present on the mirrors at XRCF.

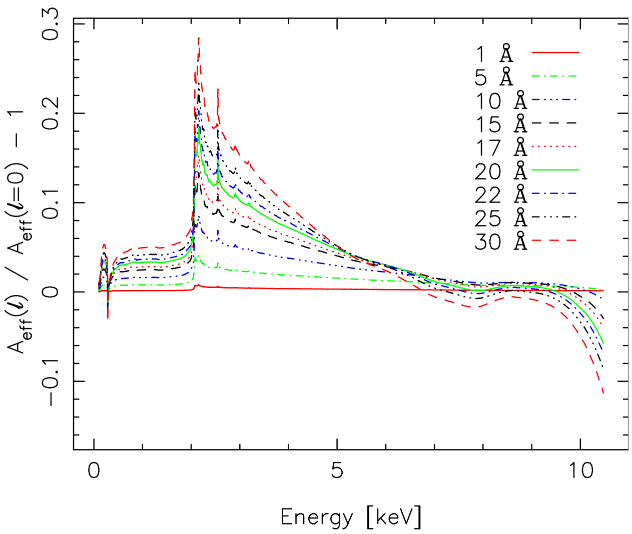

Fig. 9. The effects of an overlayer of hydrocarbon on the HRMA effective area.

3. Re-Analysis of the XRCF Data

We have re-analyzed the ground-based data and found good evidence that the overlayer was already present on the mirrors at XRCF. The fourth order polynomial empirical correction that was applied to the mirror effective area essentially corrected for the effects of the overlayer at most energies, but under corrected the effective area at the Ir-M edge. While the second correction fixed the effective area at the Ir-M edge, it over corrected the effective area at higher energies. As the depth of the contaminant increases, the slope of the effective area increases at high energies (see Fig. 9). The steeper the slope of the effective area at high energies, the greater the derived temperatures. We are still in the process of re-analyzing the ground based data. We have sufficient ground-based data to determine the depth of the contaminant on each shell separately and hope to release a new version of the HRMA effective area by early fall 2008.

Table 1. Cluster Sample and Regions used for Cross-Calibration

Name	z	N_H (10^{20} cm^{-2})	Region
A262	0.0163	5.47	annulus(01:52:46.00,+36:09:09.10,1.6′,2.7′)
			-circle(01:52:39.40,+36:07:24.20,0.5′)
			-circle(01:52:39.58,+36:10:16.51,0.5′)
A1795	0.0625	1.17	annulus(13:48:53.00,+26:35:25.00,1.5′,2.7′)
A2029	0.0773	3.14	annulus(15:10:56.20,+05:44:40.70,1.5′,2.5′)
A2052	0.0355	2.85	annulus(15:16:44.50,+07:01:19.70,1.7′,2.5′)
A3112	0.0752	2.53	annulus(03:17:57.70,-44:14:18.30,1.5′,2.9′)
			-circle(03:18:02.40,-44:16:43.30,0.5′)
A3571	0.0391	4.11	circle(13:47:28.60,-32:51:54.80,2.1′)
MKW3S	0.0450	3.05	annulus(15:21:51.40,+07:42:22.90,1.5′,2.5′)

Note. — Notes: Cluster name, redshift, galactic column density and region used to cross-calibrate between Chandra and XMM-Newton.